Hindawi
Geofluids
Volume 2021, Article ID 6697819, 16 pages
https://doi.org/10.1155/2021/6697819

Research Article

Investigating Fracture Network Deformation Using Noble Gas Release

W. Payton Gardner,[1] **Stephen J. Bauer**,[2] **and Scott Broome**[3]

[1]*Department of Geoscience, University of Montana, Missoula, MT, USA*
[2]*Geothermal Department, Sandia National Laboratories, Albuquerque, NM, USA*
[3]*Geomechanics Department, Sandia National Laboratories, Albuquerque, NM, USA*

Correspondence should be addressed to W. Payton Gardner; payton.gardner@umontana.edu

Received 21 December 2020; Revised 22 March 2021; Accepted 20 April 2021; Published 19 May 2021

Academic Editor: Orlando Vaselli

We investigate deformation mechanics of fracture networks in unsaturated fractured rocks from subsurface conventional detonation using dynamic noble gas measurements and changes in air permeability. We dynamically measured the noble gas isotopic composition and helium exhalation of downhole gas before and after a large subsurface conventional detonation. These noble gas measurements were combined with measurements of the subsurface permeability field from 64 discrete sampling intervals before and after the detonation and subsurface mapping of fractures in borehole walls before well completion. We saw no observable increase in radiogenic noble gas release from either an isotopic composition or a helium exhalation point of view. Large increases in permeability were observed in 13 of 64 discrete sampling intervals. Of the sampling intervals which saw large increases in flow, only two locations did not have preexisting fractures mapped at the site. Given the lack of noble gas release and a clear increase in permeability, we infer that most of the strain accommodation of the fractured media occurred along previously existing fractures, rather than the creation of new fractures, even for a high strain rate event. These results have significant implications for how we conceptualize the deformation of rocks with fracture networks above the percolation threshold, with application to a variety of geologic and geological engineering problems.

1. Introduction

Measuring and understanding deformation, strain, and fracturing in rocks with preexisting fracture networks is important for a variety of applications in earth sciences including earthquake monitoring, slope and tunnel stability, nuclear waste isolation, and unconventional oil and gas production. However, complex deformation mechanics and the inherent difficulty of instrumenting subsurface locations result in large uncertainty in the mechanics of subsurface fracture network deformation. Innovations in measurement and interpretation methods are needed to better measure, monitor, and predict fracture network deformation mechanics.

Radiogenic noble gases are produced by radioactive decay of naturally occurring U and Th in crustal materials. These gases accumulate in minerals grains, intergranular boundaries, and pore fluids of crustal rocks [1]. These nobles gases are likely released as a result of episodic fracturing and brittle deformation in the subsurface [2, 3]. Recent research has shown that radiogenic noble gases released from rocks as they are deformed can be observed [4–8]. Thus, monitoring noble gas release and isotopic composition could provide a new method of measuring and inferring subsurface deformation mechanics.

Noble gas emissions and their relationship to crustal-scale deformation have been studied for many years. There is a clear relationship between noble gas signatures, tectonics, deformation, and fracturing at the crustal scale [2, 3]. Helium isotope composition in the Basin and Range is correlated to tectonic velocity and provides a qualitative estimate of deep crustal permeability due to fracturing [9]. Signatures of mantle helium can be found throughout the tectonically active western U.S., indicating pervasive fracturing and faulting in the deep crust to deliver mantle helium to the shallow crustal

system [10]. Radon anomalies have been reported before earthquakes [11–13]. Postseismic changes in helium isotopic composition have been observed in spring water [14]. Radon and thoron in soil gases have been observed to be affected by seismicity [15]. However, the radon and thoron signatures are not consistent between sites, sometimes decreasing [12] or sometimes increasing [16, 17] before events. The differences in noble gas signatures prior to seismic and volcanic events are likely due to different stress, strain, and deformation mechanics prior to and during events [18].

Under uniaxial compression, radon exhalation rates have been shown to decrease during the initial compressional phase, increase as a result of microfracturing during later elastic compression, and show a long-term increase after specimen failure and macrofracturing [18–21]. Radiogenic ^{4}He and ^{40}Ar release has been shown to be highly sensitive to triaxial deformation [4, 5] and show a similar pattern to Rn, with (1) constant or slightly lower gas release during initial compression, (2) increasing gas release after reaching around 1/3 of the ultimate yield stress due to microfracture during compression, and (3) rapidly increasing gas release just before and during macrofracture, subsequently dropping after macrofracture [5, 7]. The gas release signal size has been shown to change as a function of rock type and as a result of deformation style [4–6]. These noble gas release signals have been used to infer changes in rock flow and transport properties due to fracture creation at the lab scale, using dynamic fracture flow models and matching to ^{4}He release signals [7].

Dynamic changes in radiogenic noble gas release have been observed in carefully controlled field settings. Rapid changes in stress due to fluctuations in the hydrologic load caused by large, rapid reservoir level fluctuations have been shown to result in fluctuations in radon concentration in tunnels beneath the reservoir [22]. Recently, increases in ^{4}He and ^{40}Ar in fracture fluid were observed in a carefully controlled hydraulic fracturing experiment in Switzerland providing the first observations of ^{4}He and ^{40}Ar release in the field at the scale of ~10 m from individual defined and controlled hydrofracturing events, indicating that noble gases can be used to sense fracturing in field settings [8]. To date, however, experiments of deformation in fractured media with a preexisting fracture network are nonexistent, and little is known about how the degree of preexisting fracture connectivity or the style and type of fracturing and strain accommodation would affect the noble gas signal.

Here, we report on an investigation of noble gas release before and after a large-scale deformation event due to subsurface detonation. Observations of noble gas isotopic signals, ^{4}He exhalation, and subsurface permeability are combined and interpreted to infer fracture network deformation characteristics. This paper describes the second field experiment of noble gas release during deformation after Roques et al. [8], with a significantly different deformation mechanism, strain rate, and preexisting fracture network. We use noble gas release as a novel indicator to interpret deformation mechanics in rocks with preexisting fracture networks above the percolation threshold and provide important evidence for conceptualizing the deformation of fractured rock networks. The observations here can be used to further understand noble gas release from deformation in the field and lead us one more step toward the use of noble gas release as a signal to trace mechanical deformation in geological settings.

2. Study Site

The study was located within the Energetic Materials Research and Testing Center (EMRTC) in Socorro, NM (34°03′32.6″N 106°57′22.7″W), and was chosen for the ability to utilize explosive materials, accessibility, availability of power and water, and a characterized lithology. Figure 1 shows the location of the Blue Canyon Dome (BCD) testbed in relation to the EMRTC test site and the state of New Mexico. The study site is located in the Rio Grande Rift tectonic province at ~1860 m above sea level (~427 vertical meters above the Socorro valley) on the shoulder of Blue Canyon Dome rhyolite flow, which is an 11 Mya Dacite member of the Socorro Peak Rhyolite. Boreholes were drilled in an undeveloped area on a flat ridge to the south of the peak, where no preexisting boreholes exist. Experimental boreholes were drilled primarily in the Luis Lopez Formation, which consist of rhyolitic volcanics of the ~30 Mya Mogollon-Datil volcanic field (Chamberlin 1999, Chapin 2004). Borehole logs indicate that 10 m of Miocene fanglomerate derived from Mogollon-Datil volcanics overlays the Oligocene welded rhyolitic tuff. The welded tuff extends below the maximum borehole depth of 76 m to a depth of at least 121 m below the ground surface. Outcrops of the Miocene fanglomerate deposits are exposed on the north side of the ridge, just downslope of the drilling area, and show significant fracturing at near vertical and horizontal orientations with an approximate spacing of ~0.5 m (Figure 2). These outcrop fracture patterns appear to be consistent with the predominant subsurface fracture orientation in both the fanglomerate and rhyolitic formations from borehole camera observations.

The climate of the area is classified as a cold arid steppe [23]. The mean annual precipitation at Socorro for the last 30 years is ~22.9 cm, with the majority of precipitation falling during July-October as afternoon thunderstorms. The mountains above Socorro receive more moisture than the adjacent valleys [24]. Wells drilled at the site are completed in the vadose zone (i.e., above the local water table at the site).

Previous laboratory experiments on samples of the Blue Canyon Dome rhyolite have shown reproducible, consistent radiogenic helium release as a result of deformation [25]. Helium release is dependent upon the initiation of new fracturing and is only observed when the deformation is sufficient to cause an increase in acoustic emissions [25]. These laboratory experiments indicate that radiogenic gases should be released from deformation causing the creation of new fractures in the Blue Canyon Dome rhyolite.

3. Testbed Configuration

The experiment utilized 9 new boreholes, each drilled with an air-powered hammer drill with a configuration shown in Figure 3. The ground zero (GZ) borehole, which is used for the explosions, is 25.4 cm in diameter, 76.2 m in depth,

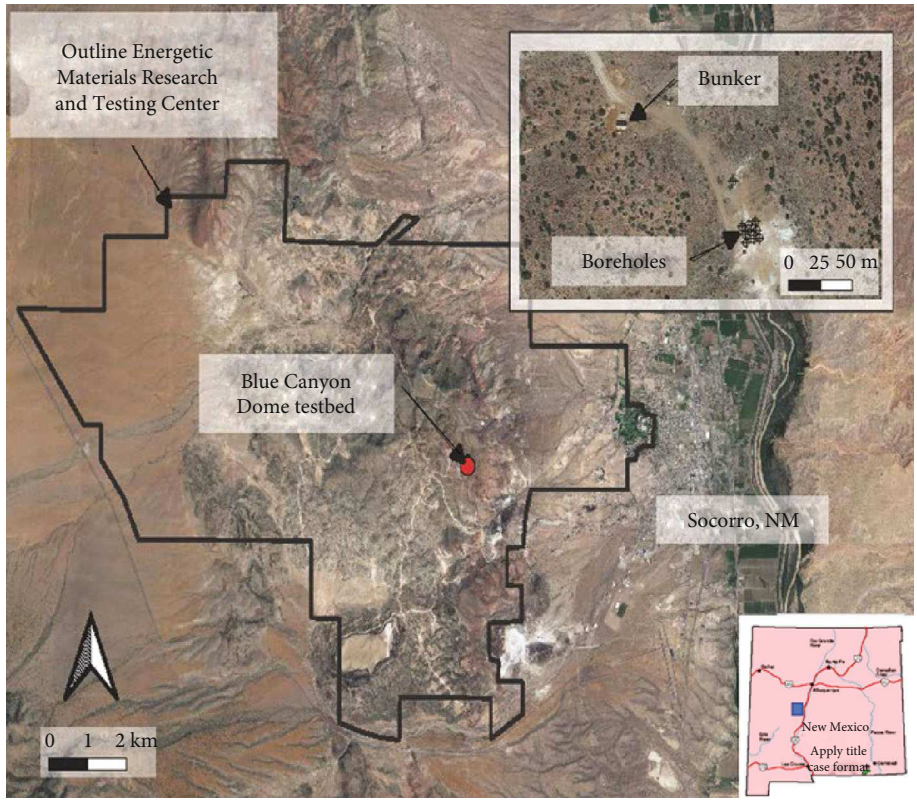

Figure 1: Map of the study area location.

steel-cased to 24.4 m, and topped with a Class 1500 flange tree. The other 8 observation boreholes are all 15.24 cm in diameter and cased to 6.1 m with PVC. There are four monitoring boreholes at a radius of 4.6 m from the GZ borehole along cardinal directions (dubbed N, E, S, and W) and another set of 4 at a radius of 7.6 m, rotated 45 degrees from the first set (dubbed NE, SE, SW, and NW).

The eight boreholes surrounding GZ (N, NE, E, SE, S, SW, W, and NW) were completed with eight discrete gas sampling locations in each well. Discrete intervals were created by pouring repeated layers of grout, sand, and epoxy (Figures 3 and 4); depths reported are approximate. Individual 0.635 cm diameter nylon tubing was terminated with a 15.24 cm screened, 0.635 cm diameter, soil vapor sampler from Geoprobe (Figure 4) that was run to each coarse sand sampling interval. Each sand layer was capped with 25.4 cm of rubberized epoxy, and then the borehole was filled with grout to the next sampling point to isolate each location. Gas sampling tubes consisted of 0.635 cm nylon tubing with stainless steel Swagelok fittings. Each gas sampling interval also included an additional "downgoing" gas tube which allowed for both induced pressure gradient and recirculated no pressure gradient sampling (Figure 4).

The deformation source was a conventional chemical explosive. The GZ borehole was filled with water to the surface the day before the shot and maintained full until the detonation by continuously pumping ~38 slpm into the borehole. The explosive package was strung using a wireline at a depth of 59.1 m, the well tree was sealed, and the package was detonated in the water-filled shot hole. The 20.2 MJ detonation generated high shock pressures causing explosive container fragmentation along with adjacent rock crushing at the wellbore wall. The explosion pressurized water in the shot hole, and gas was generated during the explosion that added to the water pressurization. The expected elastic radius was ~5 m, meaning that all borehole sampling regions within this radius were expected to be in the zone of rock failure and permanent deformation.

4. Measurement Methods

Prior to borehole completion, borehole cameras were used to take a video of the entire borehole length and visually log each borehole. Borehole recordings were used to visually map lithology and fracture location and orientation. Examples of identified fractures are shown in Figure 5. Fracture depth, orientation, and approximate fracture density were recorded for each borehole.

We measured air yield as a proxy for subsurface gas permeability in each discrete sampling interval. Air yield was measured by pumping each interval with a diaphragm gas pump at 32 standard L/min and measuring the resulting flow rate using thermal conductance air flow meters. We utilized a bank of mass flow meters with maximum flow rates of 10, 50, 500, 4000, and 20,000 standard cm^3/min (sccm) (Figure 6). Each interval was pumped until the air flow reached a steady state, usually taking around 1 hour to stabilize. The flow rate was logged using the flow meter with a midrange closest to the measured value.

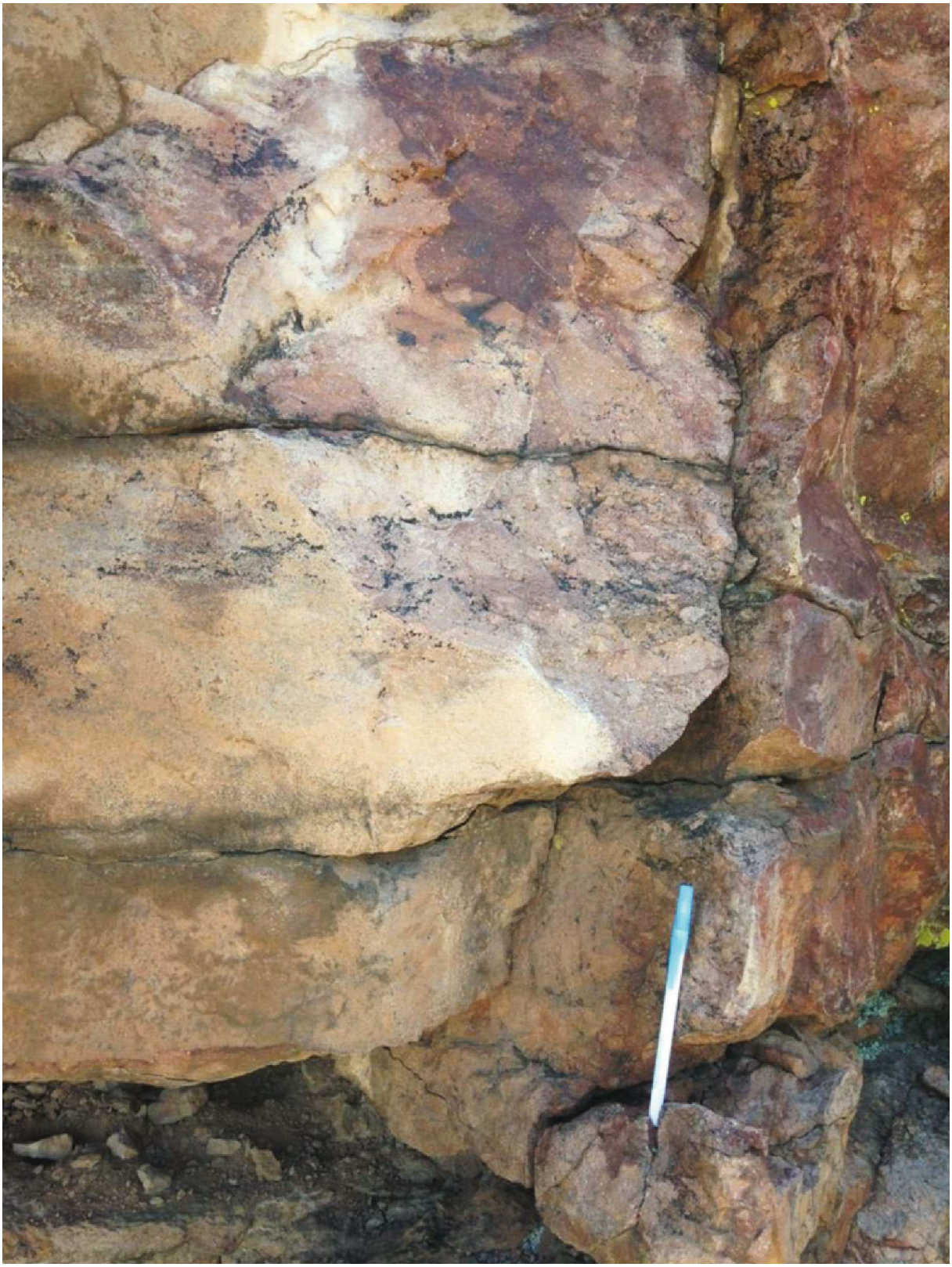

Figure 2: Outcrop of metasomatized fanglomerate exposed 100 m downslope of the testbed site.

To sample in situ dynamic noble gas isotopic signals, a high-flow diaphragm pump (the same pump used for air yield measurements) was used to pump air from 8 different sample ports in parallel to a mass spectrometer system located in an air-conditioned portable laboratory trailer roughly 40 m away from the well nest. Tubing for the gas

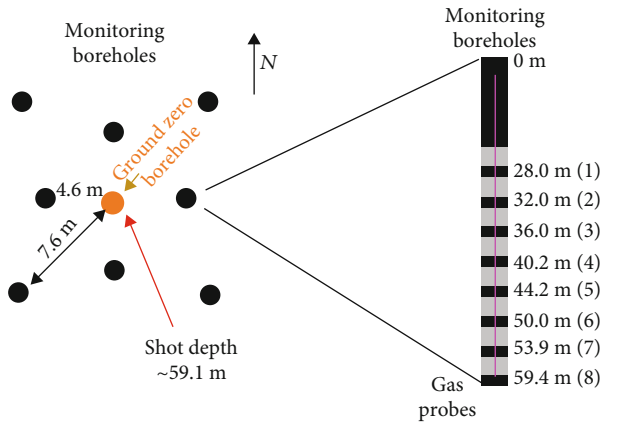

FIGURE 3: Map view (left) and cross-section (right) of the GZ borehole and 8 monitoring boreholes with locations of gas samplers. Yellow zones are zones of sand and epoxy which hold the gas sniffers. Gray zones are grout. Not to scale, grout layers are 5-7 times the height of the sand/epoxy layers.

delivery system from the borehole manifold to the pump above ground was 0.3175 cm nylon to increase fluid velocity and decrease instrumental response time. Sample port locations and depths for all sampled intervals are given in Table 1. The gas delivery system could be intermittently switched to pump directly from the atmosphere using manual valves at a tee located near the well manifold. Gas exhaust from the delivery pump was not connected to the downgoing recirculating tube; thus, the sampling interval was underpressured with respect to the surrounding reservoir during sampling. In this configuration, the induced pressure gradient caused subsurface gas to flow toward the sampling locations.

Figure 7 shows a schematic of the sampling apparatus for measuring in situ downhole noble gas isotopic composition. A water trap volume, cooled to -30°C, was put on the gas delivery line to reduce the risk of water from the detonation entering the mass spectrometer and as an initial drying stage to reduce the water vapor pressure in the gas stream. Gas from the delivery tube was sampled by the mass spectrometer system via a vacuum leak valve. A cold finger located near the leak inlet, cooled to liquid nitrogen temperature, was used as a vapor pump to reduce the partial pressure of water vapor in the mass spectrometer. The leak valve inlet was adjusted until the internal pressure was around 5×10^{-5} mbar as measured by the hot cathode gauge in the mass spectrometer vacuum chamber. The gas delivery pump was put downstream of the gas inlet to reduce pressure at the mass spectrometer inlet, thus decreasing the inlet response time. The inlet pressure was generally between 300 and 400 mbar. Assuming laminar flow, 150 m of 0.635 cm tubing, and our pumping speed of 32,000 sccm, we calculate a mean travel time of ~10 seconds from the tubing inlet to our pump using the Hagen-Poiseuille equation. Assuming an internal volume of 1 cm^3 for the leak valve, a steady mass spectrometer chamber pressure of 1×10^{-5} mbar, a steady inlet pressure of 400 mbar, and steady-state gas flow, we calculate the residence time in the leak valve inlet to be ~3 minutes. Thus, our system measures the average gas composition being pumped over a 3-minute interval. The mass spectrometer used for the analyses was a Pfeiffer HiQuad™ 300 with a crossbeam source and electron multiplier.

All masses analyzed were detected using the electron multiplier. All masses analyzed were within the operable range of the electron multiplier. Given the small variation in gas composition from atmospheric composition, the electron multiplier is expected to be approximately linear and sensitive to detecting differences from atmospheric gas composition [26]. The ion source and mass spectrometer detector settings were tuned in the field before the start of analyses. A mass scan after in-field tuning is shown in Figure 8. The important peaks for this paper are at mass 4 (^{4}He) and at mass 36 (^{36}Ar). An atmospheric standard was run at the beginning of each day and/or before and after each downhole sample. Downhole samples were run for (1) background subsurface gas preshot, (2) subsurface gas during the shot, and (3) subsurface gas postshot. The subsurface samples were pumped for a minimum of 4 hours and a maximum of nearly 21 hours.

Two background measurement sequences were made. On August 26th, 2019, an initial standard was run, followed by a downhole measurement and finally a final atmospheric standard. On the 27th, a background measurement sequence, identical to the previous day, was made, but downhole gas was collected continuously during a small test shot, where an insignificant amount of explosive was detonated to test system functioning and provide a dress rehearsal for site safety protocols.

Helium exhalation was measured from a single low-permeability interval near the detonation location (East, Lift 7). Exhalation was characterized by the produced helium flow rate during vacuum pumping as measured by a Leybold helium leak detector after [7] (Figure 9). Similar to the quadrupole gas delivery system, gas was transported from the wellhead to the leak detector using 0.3175 cm nylon tubing. A water trap at -50°C was kept in line to prevent water contamination to the leak detector. The helium flow rate measured by the leak detector was logged at 1 Hz, providing a high-resolution record of helium production.

We collected 12 discrete gas samples from the pump discharge for comparison with our real-time dynamic measurements. Samples were collected in 0.95 cm diameter soft copper tubes, 30 cm in length (internal volume = 21 cc), and sealed with refrigeration clamps. Gas from the pump discharge was allowed to flow through the tube for at least one minute. After this time, a secondary vent valve was opened on the upstream side of the copper tube, with sample gas flowing through both discharge vents; the downstream copper tube clamp was closed first, diverting all pump discharge to the secondary outlet. Finally, the upstream clamp was closed isolating the sample in a helium leak-tight vessel. This sampling procedure allowed us to collect sample gas at a pressure slightly above the ambient atmospheric pressure, with no atmospheric contamination, while at the same time keeping the pumping speed constant for dynamic gas sampling. Discrete samples were then analyzed for noble gas isotopic composition using static mass spectrometry by the

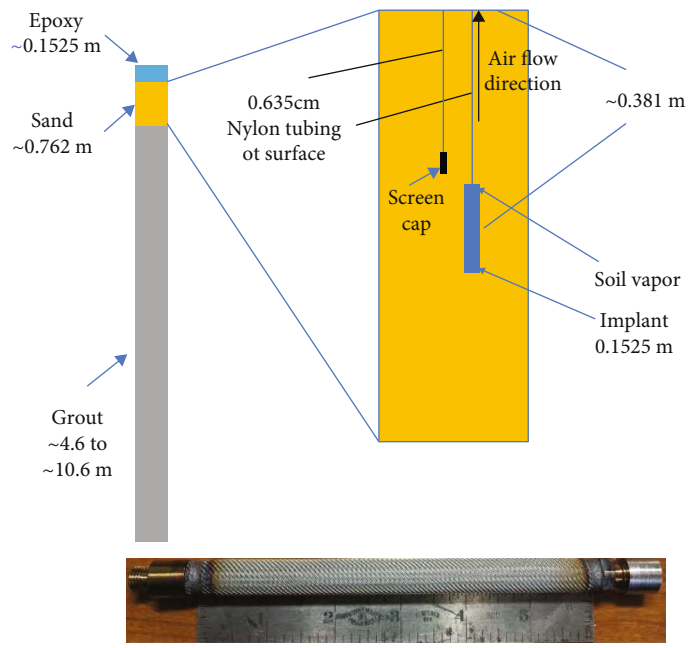

Figure 4: Close-up of the discrete sampling interval setup (top) along with a photo of the soil vapor implant (bottom).

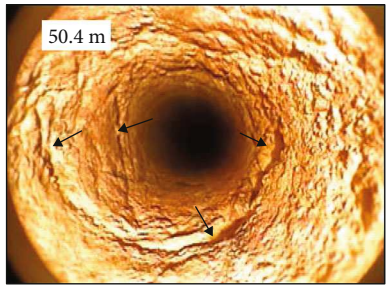

Figure 5: Preshot image of North at depth of Lift 6: high preshot flow; arrows point to large fractures.

Earth and Planetary Sciences Department Volatiles Laboratory at the University of New Mexico.

5. Results

Separate lab measurements were made to determine the helium permeability (k at 1.38 MPa confining pressure) and basic mechanical properties (unconfined compressive strength (UCS), density (ρ), tensile strength (σ_T), Young's modulus (E), and Poisson's ratio (μ)) of the rhyolite and grout (Table 2). The rhyolite is stiff and has high strength, and its matrix is low$k$, whereas the grout is soft and weak and has low permeability and high electrical resistivity. The low matrix permeability implies that flow measurements made are dominated by fracture aperture and connectivity.

5.1. Noble Gas Isotope Results. For the quadrupole analysis, the primary goal was to assess dynamic changes in the relative concentration of ^{4}He in gas pumped from underground. We quantify the relative concentration of ^{4}He in the gas phase using an atmospheric normalized fractionation factor:

$$F\left(^4He\right) = \frac{\left(I\left(^4He\right)/I\left(^{36}Ar\right)\right)_{samp}}{\left(x\left(^4He\right)/x\left(^{36}Ar\right)\right)_{ATM}}. \quad (1)$$

where $I(^iX)$ is the measured intensity of the isotope ^iX on the quadrupole, and $x(^iX)$ is the known mole fraction of the isotope ^iX in the atmosphere. ^{36}Ar was used to normalize as it has a purely atmospheric source and should not be affected by geogenic gas release.

The "intensity" measured by the quadrupole is the current generated at the detector due to the impingement of ions at the mass to charge ratio allowed through the mass filter. Given a perfect mass spectrometer, the ratio of measured intensities should be equal to the ratio of mole fractions in the gas sample. However, ionization competition or incomplete ionization of all molecules will have a larger effect on lower-concentration gases. If absolute concentration measurements are required, upstream mass separation is required to reduce ionization competition; however, relative changes in the amount of ^{4}He can be accurately assessed via the fractional factor.

Figure 10 shows the dynamic $F(^4$He) for the background well gas measurement sequence. An initial atmospheric standard was run, followed by the inlet of gas pumped from underground and then a final atmospheric standard. $F(^4$He) for the initial standard was relatively constant with a median value of 0.53. After the atmospheric standard, the inlet was changed to the well manifold and underground gas was pumped for ~4 hours. After ~1 hour, a systematic rise in $F(^4$He) was seen until stabilization at 0.72. The median value for the entire background measurement was

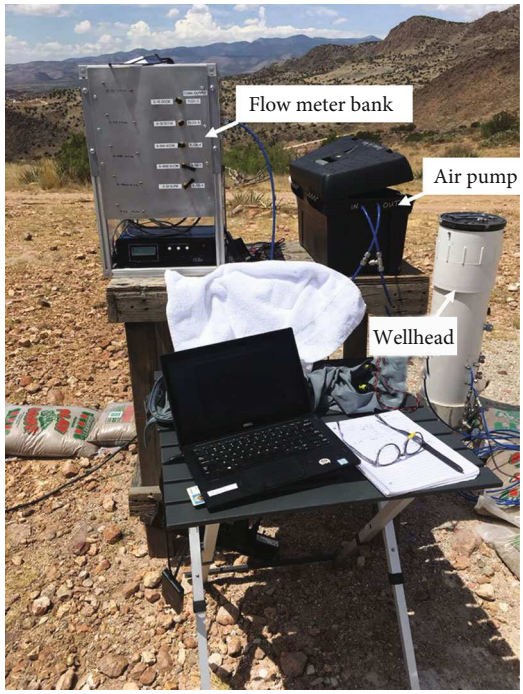

Figure 6: Photo of air flow sampling equipment and wellhead.

Table 1: Summary of sampled lift location and air flow.

Well	Lift #	Depth (m)	Distance from the GZ borehole (m)	Initial flow (sccm)	Change in air flow (sccm)	Fracture observed in near depth
N	7	53.9	6.94	500	0	No
N	8	59.4	4.61	500	0	No
NE	8	59.4	7.61	700	0	Yes
SE	8	59.4	7.61	100	2000	Yes
S	8	59.4	4.61	<100	6000	Yes
SW	8	59.4	7.61	100	100	Yes
W	7	53.9	6.94	<100	0	Yes
NW	8	59.4	7.61	600	2000	No

0.69. The subsequent ending air standard stayed constant over the measurement interval with a median value of 0.73.

Figure 11 shows whisker boxes summarizing the statistics of the entire time series for each measurement interval shown in Figure 10. The instrumental drift, likely caused by fairly large temperature variation in the trailer over the day and differences in the instrumental sensitivity at different masses, is represented by the change in the atmospheric standards. The median measurement of the background in the sample intervals falls within the drift measurement, and the well gas appears to be indistinguishable from atmospheric air. Indeed, after leveling near an $F(^4\mathrm{He})$ of 0.73, the switch between well gas and atmosphere produced no change in observable gas composition. The instrumental drift could be explained by temperature

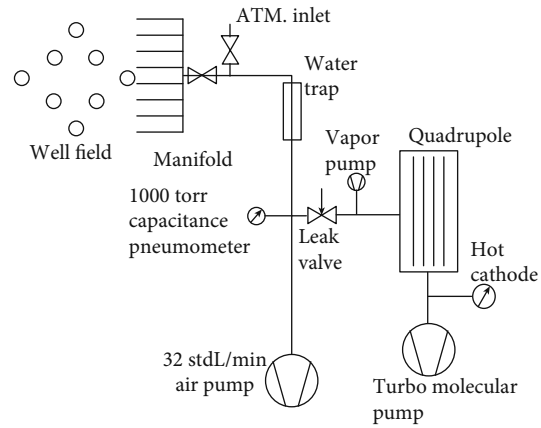

Figure 7: Schematic of the dynamic noble gas composition measurement system.

variations in the laboratory trailer and in the ambient temperature outside. The change does appear to mostly occur within 1.5 hours from 13:00 to 14:30.

Figure 12 shows the dynamic $F(^4\mathrm{He})$ for the test shot background sequence. An initial atmospheric standard was run, followed by the inlet of gas pumped from underground during the test shot, and then a final atmospheric standard was run at the end of the day. The $F(^4\mathrm{He})$ for the initial standard showed significantly more variation than the initial standard for the background measurement sequence. The atmospheric $F(^4\mathrm{He})$ bounced around a median value of 0.56. After about 1 hour of the atmospheric inlet, the value fell to ~0.48 and remained fairly constant. After the switch to the well gas, the underground gas was pumped for ~4 hours. After ~0.25 hours, a systematic rise in $F(^4\mathrm{He})$ was seen until stabilization at 0.69. The median value for the entire test shot measurement was 0.64. The ending air standard stayed constant over the measurement interval with a median value of 0.64.

Figure 13 shows whisker boxes for the statistics of the entire time series of each measurement in the test shot background measurement sequence. For the test shot sequence, the median measurement of the wells is slightly higher than either standard. However, a significant portion of both distributions overlaps, and it appears that once again, the well gas is indistinguishable from atmospheric air. No major, long-term changes in gas composition are recorded after the test shot. There is a short anomaly near 12:00, about 15 minutes after the test shot, but the abrupt change and lack of long-term persistence are more indicative of noise. After leveling near an $F(^4\mathrm{He})$ of 0.6, the switch between well gas and atmosphere produced no large change in observable gas composition. Much like the previous background gas test sequence, the change does appear to mostly occur within 1.5 hours from 10:30 to 12:00.

Figure 14 shows the dynamic $F(^4\mathrm{He})$ for the full explosion well gas measurement sequence. The $F(^4\mathrm{He})$ of the initial atmospheric standard shows the now typical increase in $F(^4\mathrm{He})$ beginning about 10:00 with a median value of 0.40. This value was also lower than those observed for previous

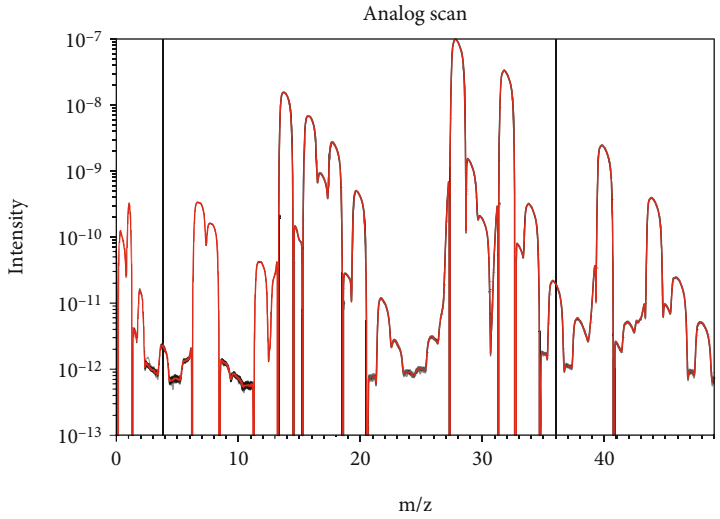

Figure 8: Analog scan of ion current intensity as a function of the mass to charge (m/z) ratio for the local atmosphere using the tuned ion source.

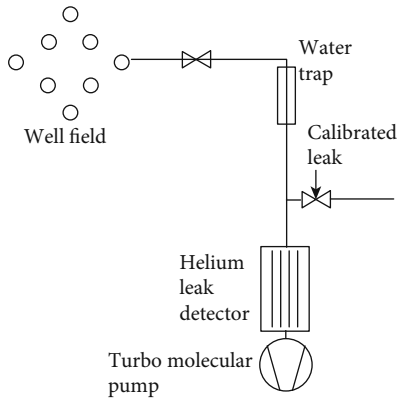

Figure 9: Helium exhalation apparatus schematic. Leybold leak detector internal vacuum schematic not detailed.

measured standards. The second standard, run immediately after the shot, had a median value of 0.39, similar to the previous standard. The postshot well gas inlet was carried out for 21 hours after the shot. The well gas composition was relatively constant over the 10 hours, then dipped and finally climbed from 09:00 to 13:00 the following day. The overall mean of the well gas over the 21-hour period was 0.50. The final ending value was around 0.53. After switching to the final atmospheric standard, the $F(^4\mathrm{He})$ value did drop slightly to a value of 0.52 and remained fairly constant.

Figure 15 shows whisker boxes for the time series of the initial standard, postshot/no-water trap well gas, and final atmospheric gas in the pre- and postdetonation measurement sequence. The median measurement of well gas postdetonation falls between both standard medians, and a significant portion of the distributions overlaps. There was a slight but observable drop in $F(^4\mathrm{He})$ after switching from the well gas to the atmospheric standard at the end of the sequence, and the well gas composition does fall above a rough linear drift estimated by the black line connecting the standard medians above the 25$^{\mathrm{th}}$ percentile (Figure 15).

Argon data show similar trends and patterns to helium. Figure 16 shows the atmosphere normalized $^{40}\mathrm{Ar}/^{36}\mathrm{Ar}$ ratio ($F(^{40}\mathrm{Ar})$) for the main shot sequence. The data largely track the changes observed in helium elemental composition. A small rise in $F(^{40}\mathrm{Ar})$ can be seen after the shot. No change in argon isotopic composition is observed after switching to the atmospheric standard at the end of the analysis.

Discrete gas sample data are summarized in Table 3. The average argon concentration (dominantly $^{40}\mathrm{Ar}$) of discrete sampled atmospheric standards was 9314 ppm. The background well gas had an average argon composition of 9424 ppm, and the well gas postshot had an argon concentration of 9464. The difference between all sample groups is within the analytical error of 191 ppm. One sample, PS-5, had a significantly higher Ar concentration, above the detection limit. Argon 40 to Argon 36 measured in the grab samples are within analytical detection of the atmospheric standard except for PS-5.

The average helium concentration for all sampled atmospheric standards was 4.33 ppm. The average helium concentration of downhole gas prior to the shot was 4.2 ppm. The average concentration of downhole gas after the shot was 3.93 ppm. The difference between the pre- and postshot downhole gases is within the 0.7 ppm analytical uncertainty. The downhole gas is 1.02 ppm lower in helium concentration than the laboratory atmospheric samples and thus slightly but measurably lower than the local atmosphere.

5.2. Helium Leak Detector. Helium exhalation at the site before, during, and after detonation is summarized in Figure 17. The background helium leak rate was steady at 2×10^{-6} ccSTP/s (cm^3/sec at standard temperature and pressure) for >24 hours prior to the shot. Immediately after the shot, the helium leak rate fell to $\sim 7 \times 10^{-7}$ ccSTP/s. Over the course of the next 19 days, the helium flow rate gradually rose to $\sim 1 \times 10^{-6}$ ccSTP/s. Short time periods (<1 h) of

Table 2: Rhyolite and grout properties.

	ρ (g/cm^3)	Apparent gas k (μD)	UCS (MPa)	E (GPa)	μ	σ_T (MPa)
Rhyolite	2.4	Lab dry: ~2 Water saturated: ~0.02	234	58.6	0.20	18
Grout	1.6	Lab dry: 100 Water saturated: ~0.1	8	2.4	0.22	2.3

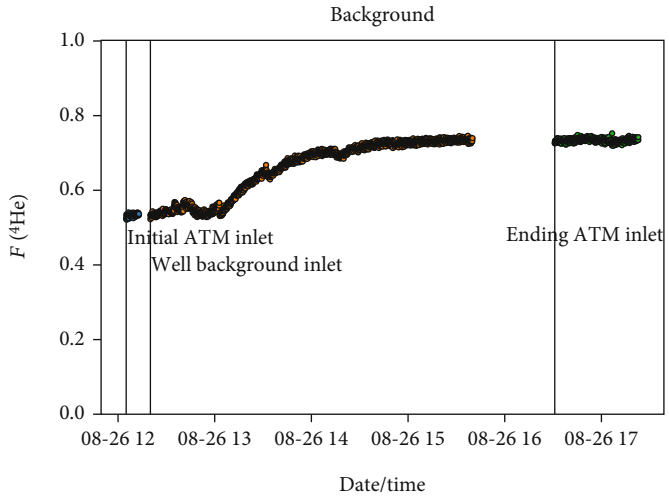

Figure 10: $F(^4\text{He})$ time series for the initial atmospheric inlet, background well gas inlet, and final atmospheric inlet. Black vertical lines indicate the approximate time of the switch to different sample inlets.

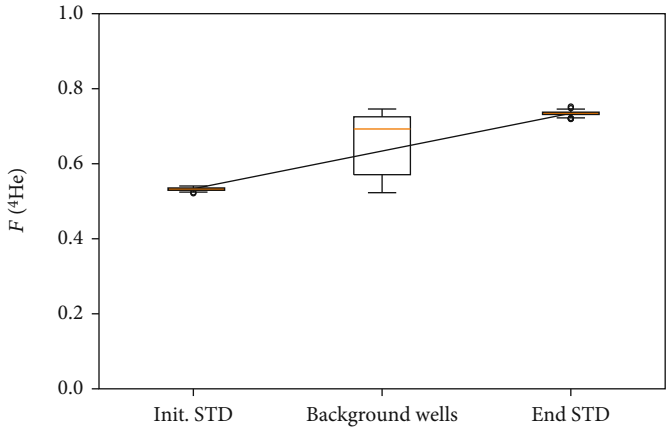

Figure 11: Whisker plots for the initial atmospheric inlet, well background, and final atmospheric inlet. A black line connects the medians of the two standards.

extreme variability in recorded data are observable at several points within the helium exhalation record. Some of these periods are associated with cleaning and reinstallation of the inline water trap; some are associated with power outages and system restarts. There are three other times with extreme variability in the flow rate recorded in the 5 days after the shot. One instance occurred during a time when water was being injected into the GZ borehole to estimate saturated hydraulic conductivity. The other two times are late in the record and are not associated with any known measurement disturbance. However, both these periods are in the afternoon-evening, during the most likely time period for monsoonal thunderstorms in the area. Given the rapid variation in the flow rate, these periods appear to be noise in the signal, which could be generated by various mechanisms during a thunderstorm.

5.3. Air Flow. Changes in measured steady-state air flow are summarized in (Figures 18 and 19). Prior to detonation, the steady-state air flow ranged from <0.1 ccSTP/m to

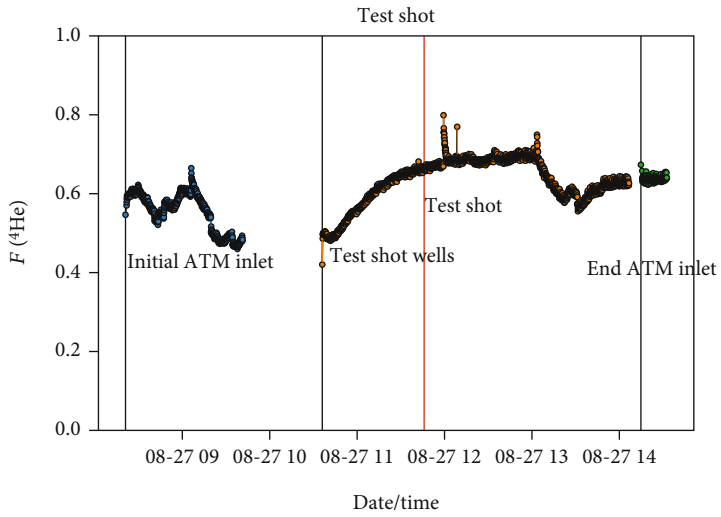

Figure 12: $F(^4\mathrm{He})$ time series for the initial atmospheric inlet, test shot well gas inlet, and final atmospheric inlet. Black vertical lines indicate the approximate time of the switch to different sample inlets. A red vertical line indicates the timing of the test shot.

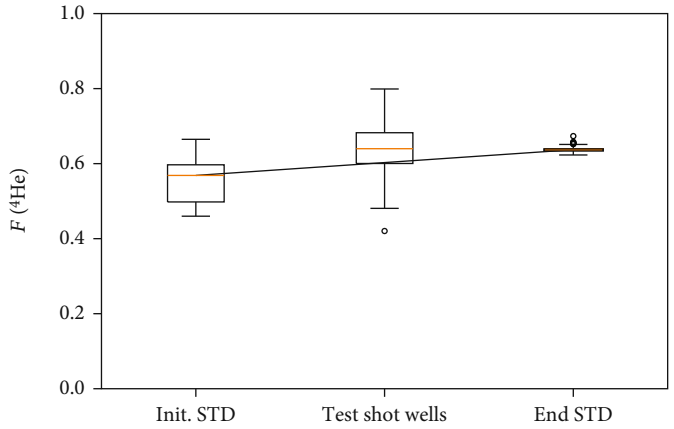

Figure 13: Whisker plots for the initial atmospheric inlet, test shot well gas, and final atmospheric inlet. A black line connects the medians of the two standards.

3320 ccSTP/m with an overall average flow rate of 276 ccSTP/m. The average value for an individual borehole from all eight sampling intervals ranged from 56 ccSTP/m to 682 ccSTP/m. Postdetonation air flow ranged from < 0.1 ccSTP/m to 7500 ccSTP/m with an overall average flow rate of 924 ccSTP/m. Individual borehole averages ranged from 400 ccSTP/m to 2200 ccSTP/m. The change in flow for discrete intervals ranged from -408 ccSTP/m to 6600 ccSTP/m with an average of 667 ccSTP/m. Borehole average flow rate changes ranged from 81.3 to 1680 ccSTP/m.

Postdetonation changes in air flow are spatially complex, with some locations recording a drop in air production and some areas showing large increases in flow. In general, air flow increases were observed to be more focused at greater depths, and all flow increases were observed in the southern half of the well network, predominantly in a southwesterly direction. Increases in flow appear to have a strong relationship with preexisting fractures. Of the 13 lifts with a reasonable increase in flow (>900 ccSTP/m), only two did not have fractures mapped. Of the 8 lifts sampled for changes in noble gas composition, 4 showed an increase in flow, only one of which did not have a fracture identified from the borehole video in the near vicinity.

6. Discussion

As a result of detonation, we see very clear indications of increased permeability at 13 of the 64 sampled discrete intervals, which provide evidence for the significant deformation of the fractured media. In contrast to the permeability measurements, we observed little to no indication of increased radiogenic noble gas release. We observed an overall decrease in helium exhalation as measured by the downhole helium leak rate. The noble gas composition of both continuously measured downhole gases and grab samples of downhole gas analyzed at an independent lab show no significant increase in $^4\mathrm{He}$ in downhole gas composition before and after the detonation. These noble gas samples included 4 intervals which had increases in flow, 3 of which saw increases over

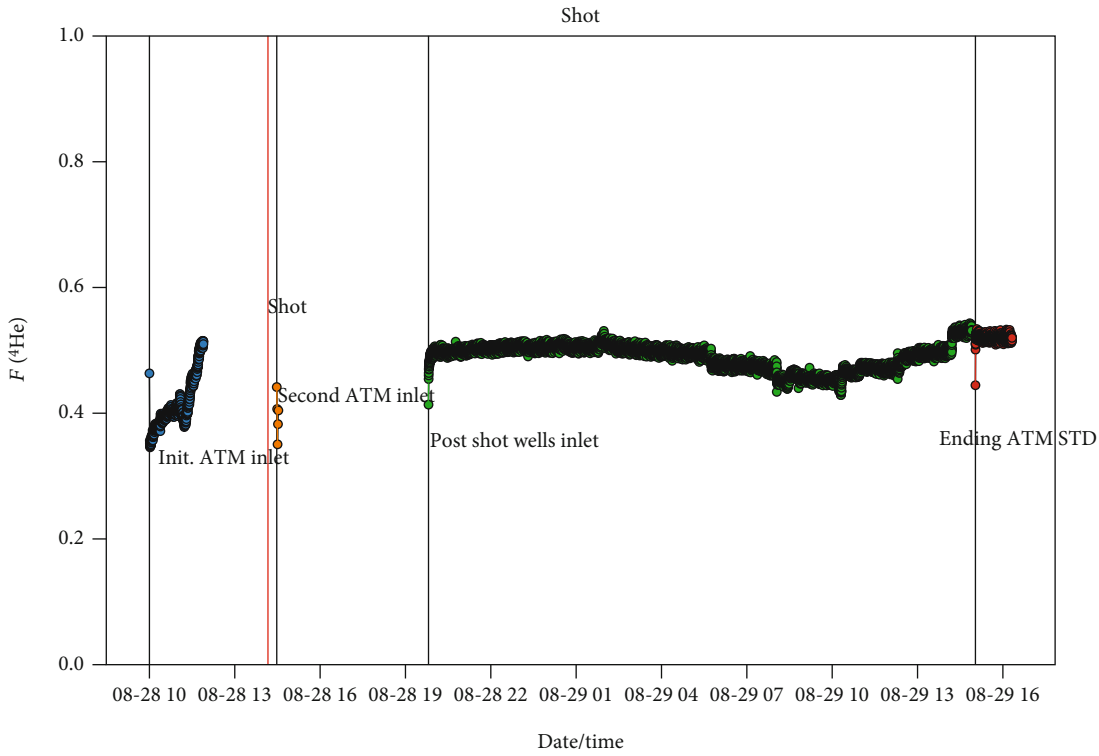

Figure 14: $F(^4\text{He})$ time series for the initial atmospheric inlet, second postshot atmospheric inlet, main shot well gas inlet, and final atmospheric inlet. Black vertical lines indicate the approximate time of the switch to different sample inlets. A red vertical line indicates the timing of the shot.

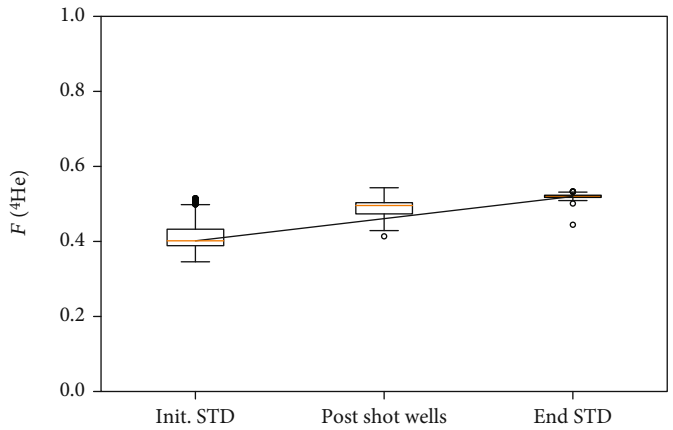

Figure 15: Whisker plots for the initial atmospheric inlet, postshot well gas, and final atmospheric inlet. A black line connects the medians of the two standards.

2000 sccm. Thus, it is clear we sampled noble gas composition from several locations that saw significant deformation.

In our experience in the lab, radiogenic noble gas release is extremely sensitive to rock deformation across a broad spectrum of rock types and deformation styles [4–7]. These experiments have shown that when new fractures are being created as a result of deformation, radiogenic noble gases are released in significant quantities. Laboratory experiments using the Blue Canyon Dome rhyolite show consistent and repeatable radiogenic helium release whenever fracturing (as indicated by acoustic emissions) is initiated. The release of noble gases from newly created fractures has recently been observed in the field at similar scales to our experiment [8]. In this experiment, individual new hydraulic fractures were created in intact matrix rock through the selective application of pressure at a focused location within the matrix alone. Radiogenic noble gases released from these new fracturing events were clearly observable in fluid discharge from preexisting fractures connected to the newly created fracture at distances of order 1 to 10 m [8]. Given this previous work, the lack of noble gas release when there is clear evidence of fracture network deformation is puzzling.

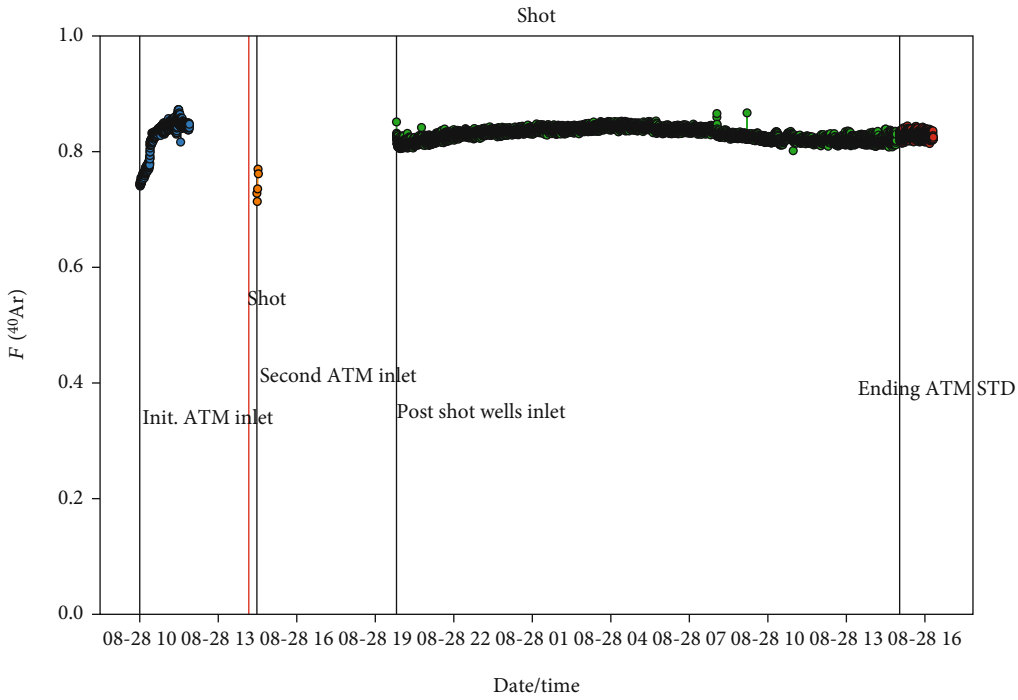

Figure 16: $F(^{40}\mathrm{Ar})$ time series for the initial atmospheric inlet, second postshot atmospheric inlet, main shot well gas inlet, and final atmospheric inlet. Black vertical lines indicate the approximate time of the switch to different sample inlets. A red vertical line indicates the timing of the shot.

Table 3: Discrete noble gas sample data.

Sample	Date	Time	Ar (ppm)	+/-	He (ppm)	+/-	$^{40}\mathrm{Ar}/^{36}\mathrm{Ar}$	+/-
(1) BCD ATM STD 1	8/21/19	09:45	9141.1	186.32	5.36	0.77	289.8	2.69
(2) BCD Well BKG 1	8/21/19	13:45	9391.2	191.41	4.16	0.60	292.9	2.72
(3) BCD ATM STD 2	8/26/19	12:15	9448.8	192.59	3.29	0.47	288.2	2.68
(4) BCD Well BKG 2	8/26/19	15:50	9390.1	191.39	4.17	0.60	291.4	2.71
(5) BCD ATM STD 3	8/26/19	17:28	9352.4	190.62	4.36	0.63	288.9	2.68
(6) BCD Well BKG 3	8/27/19	12:18	9491.3	193.45	3.61	0.52	287.9	2.67
(7) BCD Well PS 1	8/28/19	14:00	9439.6	192.40	3.97	0.57	292.2	2.71
(8) BCD Well PS 2	8/28/19	14:57	9386.2	191.31	4.52	0.65	297.1	2.76
(9) BCD Well PS 3	8/28/19	15:45	9425.6	192.12	4.26	0.61	293.5	2.73
(10) BCD Well PS 4	8/28/19	16:20	9468.1	192.98	3.71	0.53	290.6	2.70
(11) BCD Well PS 5	8/28/19	17:00	9717.3	198.06	2.87	0.41	312.4	2.90
(12) BCD Well PS 6	8/29/19	07:23	9352.3	190.62	4.19	0.60	297.3	2.76
Average STD			9314.1	189.84	4.34	0.09	289.0	2.68
Average BKG			9424.2	192.09	3.98	0.08	290.7	2.70
Average PS			9464.9	192.92	3.92	0.08	297.2	2.76

STD = standard; ATM = atmosphere; BKG = background; PS = postshot.

New laboratory results of fracture network evolution may provide some insight into the lack of noble gas release. Fractured media can deform in two different ways: (1) creation of new fractures and (2) strain along existing fractures. Renshaw et al. [27] show that when fracture networks are sufficiently connected and have reached the percolation threshold, the deformation style of the fractured media changes and permeability of the fractured media can increase without the creation of new fractures. Before percolation is reached, fracture networks are dilute and the creation of new fractures is the main mode of strain accommodation in the material. However, once the percolation threshold has been crossed, the fracture network has crossed the critical fracture density and is well connected and strain is accommodated primarily by the deformation of the existing fractures rather than the creation of new fractures [27].

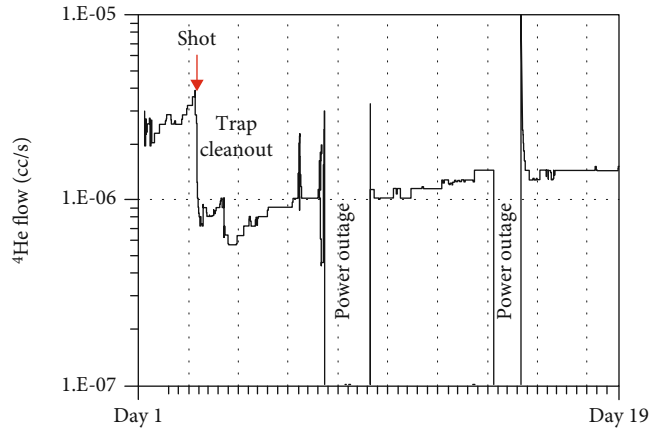

Figure 17: Helium flow sequence from the leak detector for preshot (top), shot (middle), and postshot (bottom). Data has been smoothed with a 12-minute running average filter. Data outliers from data logger disconnection have been removed.

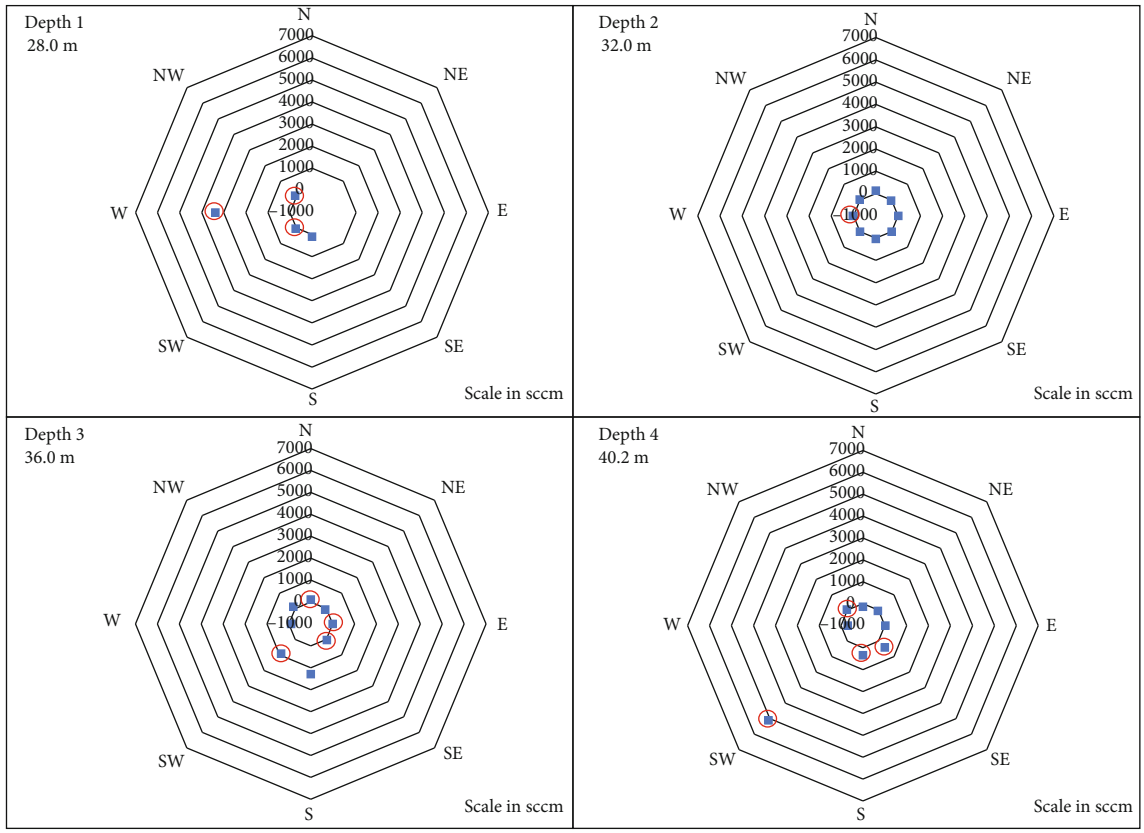

Figure 18: Postshot flow rate changes for depths 1-4. Red circles indicate stations with fractures within ~0.45 m of the station depth, observed from preshot borehole camera imaging.

Renshaw et al. [27] show that above the percolation threshold, fracture network permeability continues to increase as a function of dilation of existing fractures rather than the creation of new fractures.

Our experiment was critically different from that of [8], in that we deformed the fractured media, rather than the focused creation of new fractures. Thus, our experimental design allows for the inference of deformation mechanics of fractured rocks. The observed increase in permeability, without a coincident noble gas release, provides the first field support for the conceptual model proposed by [27], in which the deformation of fracture networks above the percolation threshold is primarily accommodated by strain on existing fractures, rather than the creation of new fractures. This result is consistent with our laboratory observations of the Kaiser effect in the Blue Canyon Dome rhyolite, which indicates that (1) helium is released whenever new fracturing occurs but (2) the onset of new fracturing is dependent upon the prior stress and strain history, and deformation without fracturing does not result in increased helium release [25].

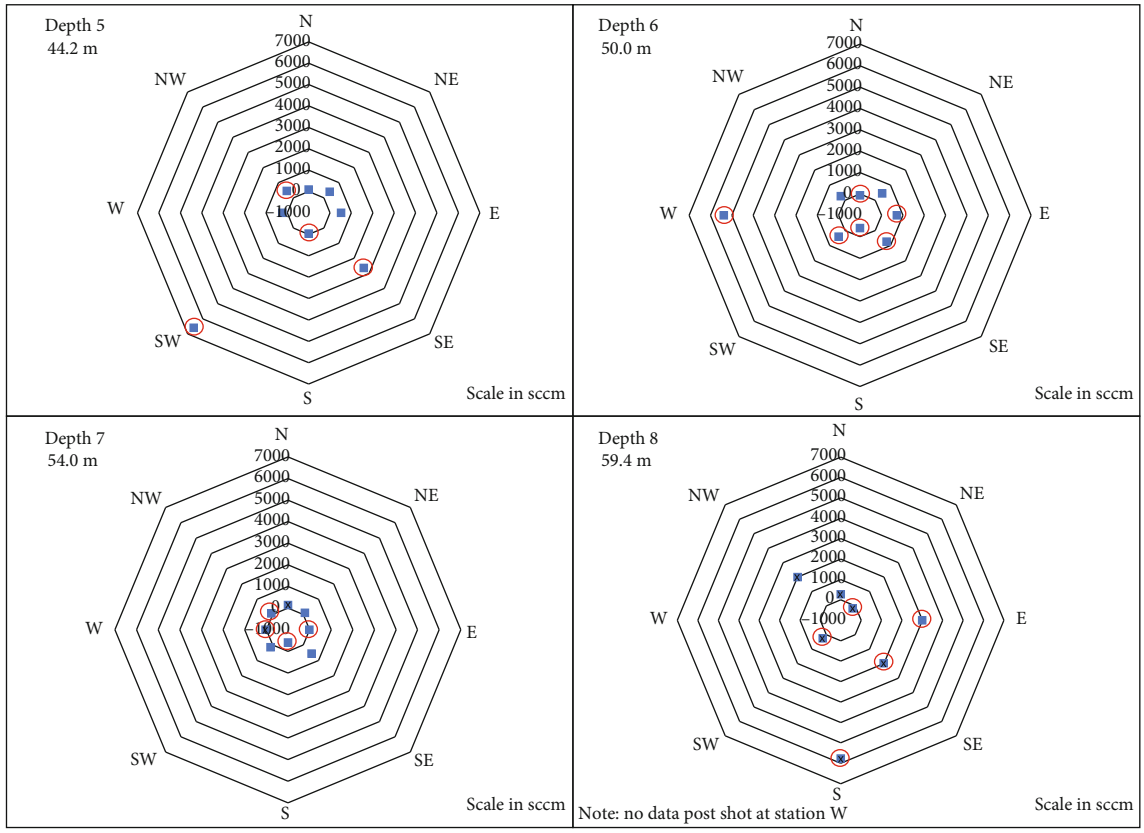

Figure 19: Postshot flow rate changes for depths 5-8. Red circles indicate stations with fractures within ~0.45 m of the station depth, observed from preshot borehole camera imaging. "X" marks intervals sampled with the quadrupole MS.

6.1. Limitations and Caveats. We are using our noble gas signal to distinguish between two conceptual models of deformation in fractured media: (1) deformation by creation of new fractures and (2) deformation along preexisting fractures. Because we cannot measure the detailed fracture network before and after detonation, we cannot definitively say how many new fractures were created as a result of the detonation. Our radiogenic noble gas signal can only be used to infer likely deformation processes. As this methodology is still relatively new, this inference is subject to increased scrutiny. However, we have now tested a variety of lithologies and ages in the laboratory setting and have found radiogenic noble release to be a sensitive indicator of new fracture creation [4–7]. Radiogenic gas release will be dependent upon the lithology and geologic history and cannot be expected for every rock type in every setting. However, radiogenic gases have been found to be released from a variety of different lithologies [5, 6, 25], and to date, we have not analyzed a lithology where radiogenic gas release was not measurable in the laboratory. In addition, new fracture creation has been linked to radiogenic noble release at similar scales in the field setting [8], lending confidence to our inference. Because mapping of 3D fracture networks at the field scale is not possible and because of the limitations of other geophysical methods in detecting preexisting vs. new fractures, noble gases may be one of the only methods available to distinguish between these two styles of deformation.

One discrete gas sample showed increased argon concentration and a higher 40/36 ratio. Our dynamic sampling did not show the same increase at this time. The helium concentration in this sample was significantly lower than the atmosphere at 2.8 ppm. It is hard to envision a scenario where radiogenic argon is released but not helium; thus, we believe this sample does not represent a radiogenic gas signal.

We were only able to sample 8 discrete locations. It is certainly possible that newly created fractures were linked to unsampled locations. To some extent, it is impossible to sample the entire 3D volume around the detonation, and thus, we can never rule out new fractures we did not sample. However, we did sample the nearest location to the detonation, which would have seen the largest transient stress due to the detonation. In addition, half of our sampled locations saw large increases in permeability, indicating there was significant deformation in our sampled zones. We can say that at least in our sampled area, there was significant deformation without the creation of new fractures.

Due to concerns about the safety of equipment, we did not run the mass spectrometer during the detonation. It is possible that radiogenic gas produced was pushed past our sampling intervals during the detonation and we missed the signal. In our experience, there are two phases of radiogenic gas release as a result of fracture—release during fracture and subsequent increased diffusive exhalation from new fracture walls after fracture [7]. It is highly unlikely that we could have created any new fractures without some signal of

increased gas exhalation. Our helium leak detector was kept running throughout the detonation and did not register any short-lived helium exhalation increase adding to our confidence. Finally, all sample locations were underpressured as a result of pumping, which would tend to direct any gas from newly created fractures back toward our sampling locations even if it was pushed past the sampling location initially.

Due to safety concerns, our detonation occurred in a water-filled borehole in the vadose zone. Thus, we have two phases present, complicating the interpretation. However, before and after detonation, all discrete intervals yielded air and not water; thus, the system was dominantly unsaturated. In addition, helium is sparingly soluble; thus, excess helium released by fracture of rocks would not be expected to be significantly attenuated by solution in water. Even if water solution was a temporary sink of helium, the mechanism would be similar to sorption and cause retardation of the helium signal, not complete removal. Once we began pumping, new gas entering the fractured rock system would be lower in helium concentration and helium would exsolve. Given the fact that we pumped air for the entire experiment and that even after long times we did not measure a helium increase, we expect that dual-phase effects here were not significant.

7. Conclusions

We report on a field experiment where we investigate the release of naturally accumulated noble gases due to large-scale deformation from subsurface detonation. We show that radiogenic gas release can provide important and complementary information on the style and type of deformation in fractured media at the field scale. We saw observable increases in gas permeability with an increase in gas yield at 13 of 64 discrete sampling locations. Of those, only two did not have a preexisting fracture visible by borehole cameras, indicating that much of the permeability increase occurred along preexisting fractures. We saw no evidence of an increase in released radiogenic noble gases in real time and grab samples. Overall, helium exhalation rates appear to have remained constant in areas with no fracture permeability, as our helium leak detector connected to a low-permeability sample port showed a reduction in helium flow after detonation with the subsequent gradual return to predetonation values. The lack of radiogenic noble gas generation, little change in helium exhalation rates, and permeability increases in locations dominated by preexisting fractures all indicate that large-scale newly created fractures were not directly connected to our sampling location. In addition, it appears that the amount of microfracture and volume damage was not enough to generate an observable radiogenic noble gas signal. We infer that most of the strain must have been accommodated by the deformation of the existing fracture network, and newly created fractures were uncommon. These results have important implications for the broader application of radiogenic noble gas release as a tracer of mechanical deformation and for the understanding and conceptualization of deformation in fractured rocks above the percolation threshold.

Data Availability

All model input and relevant output data will be archived online in the zenodo online data archive and will be available at URL: https://zenodo.org/deposit/4763385 and DOI: 10.5281/zenodo.4763385.

Disclosure

Any subjective views or opinions that might be expressed in the paper do not necessarily represent the views of the U.S. Department of Energy or the United States Government.

Conflicts of Interest

The authors declare that there is no conflict of interest regarding the publication of this paper.

Acknowledgments

The subsurface portion of the "greater" test system design, layout, deployment, and conduct was led by K. Chojnicki (SNL) and H. Knox (PNNL) before her. E. Robey is the current experiment lead and described the shot 1 detail. M. Ingraham, J. Feldman, D. King (SNL), J. Knox, C. Strickland, T. Johnson, and C. Johnson (PNNL) organized and led drilling efforts through sensor deployments; many individuals were involved in the other parts of this test setup and conduct. M. Ingraham organized and managed the main underground test. J. Hamilton (UNM) made the posttest lab-based helium measurements. P. Schwering took preshot borehole images. The EMRTC staff provided logistical field support. The underground test system deployment was intended for test objectives not directly associated with the objectives of this paper. We thank Dr. Kris Kuhlman for his technical review of this paper; his comments and suggestions improved its content. The authors acknowledge important interdisciplinary collaboration with scientists and engineers from LANL, LLNL, MSTS, PNNL, and SNL. This paper describes objective technical results and analysis. Sandia National Laboratories is a multimission laboratory managed and operated by National Technology and Engineering Solutions of Sandia, LLC., a wholly owned subsidiary of Honeywell International, Inc., for the U.S. Department of Energy's National Nuclear Security Administration under contract DE-NA-0003525. This research was funded by the National Nuclear Security Administration, Defense Nuclear Nonproliferation Research and Development (NNSA DNN R&D).

References

[1] T. Torgersen, "Controls on pore-fluid concentration of 4He and 222Rn and the calculation of 4He/222Rn ages," *Journal of Geochemical Exploration*, vol. 13, no. 1, pp. 57–75, 1980.

[2] D. Buttitta, A. Caracausi, L. Chiaraluce, and R. Favara, "Continental degassing of helium in an active tectonic setting (northern Italy): the role of seismicity," *Scientific Reports*, vol. 10, no. 1, 2020.

[3] T. Torgersen, "Continental degassing flux of 4He and its variability," *Geochemistry, Geophysics, Geosystems*, vol. 11, no. 6, 2010.

[4] S. J. Bauer, W. P. Gardner, and J. E. Heath, "Helium release during shale deformation: experimental validation," *Geochemistry, Geophysics, Geosystems*, vol. 17, no. 7, pp. 2612–2622, 2016.

[5] S. J. Bauer, W. P. Gardner, and H. Lee, "Release of radiogenic noble gases as a new signal of rock deformation," *Geophysical Research Letters*, vol. 43, no. 20, pp. 10,688–10,694, 2016.

[6] S. J. Bauer, W. P. Gardner, and H. Lee, "Noble gas release from bedded rock salt during deformation," *Geofluids*, vol. 2019, 12 pages, 2019.

[7] W. P. Gardner, S. J. Bauer, K. L. Kuhlman, and J. E. Heath, "Modeling dynamic helium release as a tracer of rock deformation," *Journal of Geophysical Research: Solid Earth*, vol. 122, no. 11, pp. 8828–8838, 2017.

[8] C. Roques, U. W. Weber, B. Brixel et al., "In situ observation of helium and argon release during fluid-pressure-triggered rock deformation," *Scientific Reports*, vol. 10, no. 1, pp. 6949–6949, 2020.

[9] B. M. Kennedy and M. C. van Soest, "Flow of mantle fluids through the ductile lower crust: helium isotope trends," *Science*, vol. 318, no. 5855, pp. 1433–1436, 2007.

[10] L. J. Crossey, K. E. Karlstrom, A. E. Springer, D. Newell, D. R. Hilton, and T. Fischer, "Degassing of mantle-derived CO2 and He from springs in the southern Colorado Plateau region — neotectonic connections and implications for groundwater systems," *Geological Society of America Bulletin*, vol. 121, no. 7-8, pp. 1034–1053, 2009.

[11] U. Tsunogai and H. Wakita, "Precursory chemical changes in ground water: Kobe earthquake, Japan," *Science*, vol. 269, no. 5220, pp. 61–63, 1995.

[12] H. Wakita, Y. Nakamura, K. Notsu, M. Noguchi, and T. Asada, "Radon anomaly: a possible precursor of the 1978 Izu-Oshima-Kinkai earthquake," *Science*, vol. 207, no. 4433, pp. 882-883, 1980.

[13] H. Wakita, G. Igarashi, and K. Notsu, "An anomalous radon decrease in groundwater prior to an M6.0 earthquake: a possible precursor?," *Geophysical Research Letters*, vol. 18, no. 4, pp. 629–632, 1991.

[14] K. Brauer, H. Kampf, G. Strauch, and S. M. Weise, "Isotopic evidence 3He/4He, of fluid-triggered intraplate seismicity," *Journal of Geophysical Research-Solid Earth*, vol. 108, no. B2, 2003.

[15] T. F. Yang, V. Walia, L. L. Chyi et al., "Variations of soil radon and thoron concentrations in a fault zone and prospective earthquakes in SW Taiwan," *Radiation Measurements*, vol. 40, no. 2-6, pp. 496–502, 2005.

[16] M. E. Cox, K. E. Cuff, and D. M. Thomas, "Variations of ground radon concentrations with activity of Kilauea volcano, Hawaii," *Nature*, vol. 288, no. 5786, pp. 74–76, 1980.

[17] P. Richon, J.-C. Sabroux, M. Halbwachs et al., "Radon anomaly in the soil of Taal volcano, the Philippines: a likely precursor of the M 7.1 Mindoro earthquake (1994)," *Geophysical Research Letters*, vol. 30, no. 9, p. 1481, 2003.

[18] F. Girault, A. Schubnel, and É. Pili, "Transient radon signals driven by fluid pressure pulse, micro-crack closure, and failure during granite deformation experiments," *Earth and Planetary Science Letters*, vol. 474, pp. 409–418, 2017.

[19] R. F. Holub and B. T. Brady, "The effect of stress on radon emanation from rock," *Journal of Geophysical Research: Solid Earth*, vol. 86, no. B3, pp. 1776–1784, 1981.

[20] S. Mollo, P. Tuccimei, M. J. Heap et al., "Increase in radon emission due to rock failure: an experimental study," *Geophysical Research Letters*, vol. 38, no. 14, 2011.

[21] P. Tuccimei, S. Mollo, S. Vinciguerra, M. Castelluccio, and M. Soligo, "Radon and thoron emission from lithophysae-rich tuff under increasing deformation: an experimental study," *Geophysical Research Letters*, vol. 37, no. 5, 2010.

[22] M. Trique, P. Richon, F. Perrier, J. P. Avouac, and J. C. Sabroux, "Radon emanation and electric potential variations associated with transient deformation near reservoir lakes," *Nature*, vol. 399, no. 6732, pp. 137–141, 1999.

[23] M. C. Peel, B. L. Finlayson, and T. A. McMahon, "Updated world map of the Köppen-Geiger climate classification," *Hydrology and Earth System Sciences*, vol. 11, no. 5, pp. 1633–1644, 2007.

[24] S. K. Anderholm, *Hydrogeology of the Socorro and La Jencia Basins, Socorro County, New Mexico*, Water-Resources Investigations Report, Reston, VA, USA, 1987.

[25] S. J. Bauer, "Observation of the Kaiser effect using noble gas release signals," *Rock Mechanics and Rock Engineering*, vol. 51, no. 2, pp. 647–651, 2018.

[26] R. E. Ellefson, "Methods for in situ QMS calibration for partial pressure and composition analysis," *Vacuum*, vol. 101, pp. 423–432, 2014.

[27] C. E. Renshaw, E. M. Schulson, D. Iliescu, and A. Murzda, "Increased fractured rock permeability after percolation despite limited crack growth," *Journal of Geophysical Research: Solid Earth*, vol. 125, no. 8, 2020.